Sensors & Actuators: B. Chemical 396 (2023) 134620

Contents lists available at ScienceDirect

Sensors and Actuators: B. Chemical

journal homepage: www.elsevier.com/locate/snb

Switchable operating modes enable low power consumption and improved gas sensing efficiency in MoS_2/BP heterojunction

Nan Zhang [a,1], Fan Tan [b,1], Liujian Qi [a], Junru An [b], Mengqi Che [b], Yaru Shi [b], Yahui Li [b], Zhiming Shi [a], Xiaojuan Sun [a], Shaojuan Li [a,*], Dabing Li [a,*]

[a] State Key Lab Luminescence & Application, Changchun Institute of Optics, Fine Mechanics and Physics, Chinese Academy of Sciences, Changchun, Jilin 130033, PR China

[b] University of Chinese Academy of Sciences (UCAS), Beijing 100049, PR China

ARTICLE INFO

Keywords:
P-n junction
Self-powering
Gas sensor
Switchable operating modes
Fast recovery

ABSTRACT

Low power consumption and reliable response are two main requirements for gas sensors to be suitable for emerging Internet of Things and Industrial Internet applications. However, state-of-the-art inorganic chemiresistor-type gas sensors have difficulty overcoming the limitations of high-power consumption. Integrating complementary photovoltaic effect and gas sensing functions in a single heterojunction is an alternative approach. Herein, we present diode-type gas sensors based on two-dimensional heterojunction, which can switch the operating modes by adjusting the bias voltage or illumination condition. At forward bias, the sensor has a high response of 310 and good selectivity, while in self-powered mode, it exhibits an open circuit voltage of 0.36 V, a fast recovery rate (27.3 s), and low power consumption (20 nW). Furthermore, the gas sensing mechanism at room temperature was confirmed by energy potential, photoluminescence, Raman spectra measurements, and the DFT calculations before and after NO_2 exposure, indicating that the electron transfer between the heterojunction and NO_2 molecules was the dominant factor. The proposed gas sensor with the switchable operating modes may open new avenues for the development of advanced energy-efficient, high-efficiency gas sensing devices, and concepts.

1. Introduction

Gas sensors have occupied a significant important position in the fields of environmental monitoring, industrial production, and indoor air quality monitoring. Among the numerous toxic and harmful gases, nitrogen dioxide (NO_2) has attracted widespread attention from international health organizations and scientific research communities [1–3]. The ongoing Internet of Things (IoT) requires even lower power consumption for high-performance sensors and smart wireless sensor networks [4]. As an important component of IoT devices, gas sensors are increasingly in demand for monitoring flammable and toxic gases without the need for an external power supply [5–7]. Although the state-of-the-art chemiresistor-type gas sensors based on traditional metal oxide have a high response, they usually require a high operating temperature range of 200–650 ℃ to ensure the rapid recovery speed, which is not suitable for the application of gas sensors in emerging application fields [8–10]. Therefore, it is of great scientific significance and social value for exploring new device architectures to improve sensor performance and expand its application scenarios.

Diodes are one of the most suitable candidates for modern electronic or optoelectronic systems and also provide a pathway for the development of advanced gas sensing technology [11]. Diode-type gas sensors are usually made from a p-n, n-n, or p-p junction that can be formed by establishing a close electrical contact at the interface between two different semiconductor materials [12]. When a contact is established between two semiconductor materials of different conduction states, the Fermi energy levels at the interface can reach equilibrium, leading to the formation of a built-in electric field [13]. In forward bias, diode-type gas sensors have a high response due to the transport of carriers at the heterojunction interface, making them more susceptible to being trapped by gas, which is similar to the mechanism of operation of chemiresistive-type gas sensors [14]; Under zero bias, driven by the built-in electric field of the heterojunction when light is applied on the heterojunction, photogenerated carriers can be effectively separated,

* Corresponding authors.
E-mail addresses: lishaojuan@ciomp.ac.cn (S. Li), lidb@ciomp.ac.cn (D. Li).
[1] Nan Zhang and Fan Tan contributed equally to this work.

https://doi.org/10.1016/j.snb.2023.134620
Received 1 August 2023; Received in revised form 6 September 2023; Accepted 12 September 2023
Available online 14 September 2023

providing low-power operation of the gas sensor [15,16]. Thus, the diode with rectification and photovoltaic effect provides a significant path for high-performance and low-consumption gas sensing. However, conventional semiconductor-based diodes require complex fabrication processes such as doping in the semiconductor, controlling the interface and thickness at the atomic scale, tuning the work function, and depositing each layer in an ultra-clean environment [17]. In addition, there are many obstacles in conventional diodes using three-dimensional (3D) bulk materials, such as lattice mismatches between materials, dislocation defects, interdiffusion, and cross-contamination, which have deteriorated the performance of the diode-based gas sensor and limits the application of diode-based gas sensors [18].

All of these key issues may be addressed with the advent of two-dimensional (2D) materials. The gas sensors based on 2D materials not only operate at room temperature but also have high sensitivity, which benefits from their unique large specific surface area and high surface activity [19,20]. Due to the action of the van der Waals forces, high-quality 2D heterojunction interfaces can be formed in the stacking region of the materials [21]. Besides, the band alignment at the interface can be precisely designed to achieve selectable gas-sensitive properties by modulating 2D materials with different band structures, charge polarities, carrier concentrations, and work functions. In recent years, various groups have conducted research on gas sensors based on 2D heterojunctions. For example, Feng and co-workers reported few-layered black phosphorus (BP)/molybdenum diselenide ($MoSe_2$) vdW heterojunctions that have 25 ppb of lower limitation of detection (LOD) and higher sensitivity to NO_2 than the sensors made of homogeneous materials at forward bias [22]. Zhang and co-workers synthesized MoS_2 p-n junction, which exhibit outstanding sensitivity to NO_2 at room temperature, as well as an extremely low LOD of 8 ppb at forward bias [23]. Besides, 2D heterojunction-based devices usually offer excellent optoelectronic properties and high photoelectric conversion efficiency, forming a series of self-powered gas sensors that are capable of detecting gases and generate readout signals without an external power supply to activate sensor-gas interactions [24]. In comparison to forward bias mode, the photogenerated carriers can be separated quickly by the built-in electric field, thus providing for a faster response and recovery rate. For instance, Niu et al. reported a NO_2 sensor based on MoS_2/GaSe heterojunction [25]. Under 405 nm visible light irradiation, the photovoltaic self-powered gas sensor showed a shorter response and recovery times for ppb-level NO_2. Through the above research, it can be found that diode-type gas sensors can operate in different modes with distinct sensing behaviors. In forward bias mode, the device exhibits high sensitivity, low lower detection limit, and good selectivity; in the self-powered mode, the sensor has a fast response and recovery rate. However, in existing device architectures, the self-powered and sensitive units are separate, which makes it difficult to combine the advantages of each in different operating modes. Therefore, achieving complementary gas-sensitive performance by integrating sensing and photovoltaic self-powered functions in a single diode is a potential way to further optimize gas-sensitive performance.

Herein, we present a new approach to low power consumption and improved gas sensing efficiency enabled by switchable operating modes in MoS_2/BP heterojunction. At forward bias, the MoS_2/BP heterojunction demonstrates promising gas-sensitive performance toward NO_2, including high response (R) of 310, high selectivity, and ppb-level LOD (104 ppb), moderate recovery time (54 s). And under visible light illumination, the heterojunction possesses photovoltaic self-powered characteristics and fast recovery speed (27.5 s), which are attributed to the rapid separation of photogenerated carriers at the heterojunction interface and the generation of electric barrier potential. In this context, we combine the two operating modes of the diode-gas sensor based on MoS_2/BP heterojunction under alternating signal stimulation in forward bias and visible light illumination. The sensor exhibits good robustness and repeatability, allowing for power consumption (20 nW), high R (310), and fast recovery time (27.5 s). The fast recovery and repeatable operation, combined with the sensitivity to low concentrations of gas, demonstrate the potential of our sensor to develop highly sensitive, sustainable, low power consumption, and reliable gas sensing platforms, expanding the sensor application scenarios.

2. Experimental section

2.1. Preparation of MoS_2 and BP nanoflakes

MoS_2 and BP nanoflakes were prepared from bulk BP and MoS_2 crystals (Six Carbon Technologies Shenzhen, China) by mechanical exfoliation method. First, MoS_2 and BP crystals adhered onto Nitto tape (Nitto Denko, Japan), and then the tape was repeatedly folded in half. The tapes with MoS_2 and BP nanoflakes were affixed with PDMS viscoelastic stamps (METATEST Corporation, China), respectively. Next, multilayer MoS_2 and BP nanoflakes were observed and selected with an optical microscope (OLYMPUS, Japan, BX53M). BP as the bottom layer of the heterojunction was accurately transferred from the PDMS stamp to the SiO_2/silicon wafer using a dry transfer platform (METATEST Corporation, China, E1-T). The multilayer MoS_2 nanoflakes were transferred to one side of the BP flakes and partially overlapped with the BP nanoflakes using the same method. MoS_2/BP heterojunctions were successfully prepared through the above steps.

2.2. Fabrication process of the MoS_2/BP p–n junction devices

Standard UV lithography was used to define metal contacts. Ti/Au (20/80 nm) was deposited on BP and MoS_2 nanoflakes using a thermal evaporator.

2.3. Characterization

The optical images of MoS_2/BP heterojunctions were obtained by the optical microscopy. AFM and KPFM images were obtained by atomic force microscopy (Oxford Instruments, Britain, Cypher S). Raman and PL spectra were tested at a laser confocal Raman microscopy excitation wavelength of 532 nm (Witec, Germany, Alpha 300r) before and after injection of NO_2 gas into an in-closed probe station (INSTEC, USA, hcp421v-pm).

2.4. Photoelectric sensing characteristics test

The photoelectric characteristics of the device were tested by using a semiconductor analyzer (Tektronix, USA, Keithley 4200 SCS) combined with the probe station. In our experiments, three irradiation lasers (FS-OPTICS, China, MW-YGX) with wavelengths of 405, 532, and 633 nm were used, and the power density of the laser is modulated by the power supply and calibrated by the laser power meter (Thorlabs, USA, PM100D).

2.5. Gas sensing characteristics test

The gas sensor measurements were carried out in the probe station. The gas sensing performance of the sensor was measured by monitoring the variation of the current (Tektronix, USA, Keithley 2636B) in the air and the target gas. The three mass flow controllers (Seven-star, China, CS-200A) were used to vary the NO_2 concentration from 0.1 ppm to 100 ppm by changing the flow ratio between NO_2 and air. The gas pressure during the measurement was 101.325 kPa. The ambient temperature during gas sensing measurement is 25 °C at room temperature. The response value (S) is defined as $S = I_0/I_g$, where I_0 and I_g are the sensor current values in air and target gas, respectively. Response time or recovery time was defined as the time to reach 90 % of the total current or response variation.

2.6. DFT Simulations

All calculations are performed by using the Vienna ab initio simulation package (VASP) with the projector-augmented wave (PAW) methods [26,27]. The Perdew-Burke-Ernzerhof (PBE) exchange-correlation is applied and the van der Waals interactions are described with the DFT-D3 method [28]. The cutoff energy of 500 eV and the Monkhorst–Pack 4 × 4 × 1 k-mesh are set for all calculations. The convergence of the total energy and the maximal residual force are set to 1.0×10^{-6} eV and 0.01 eV/Å, respectively. The vacuum layer of 20 Å is applied to prevent interactions between the periodic slabs. Well-converged and reliable results are obtained using all of the above parameters.

3. Results and discussion

3.1. Morphological and structural characteristics

We propose the gas sensor based on the MoS_2/BP diode as schematically shown in Fig. 1a. The voltage (V_{ds}) is applied across the BP terminal (Source) to the bottom MoS_2 (Drain) on the SiO_2/Si substrate. From the perspective of the device structure, the device can be regarded as a MoS_2/BP diode with two resistors in series at both ends. The schematic of the band diagrams of MoS_2/BP heterojunction under different bias voltages are shown in Fig. 1b. When the contact between n-type MoS_2 and p-type BP occurs, electrons flow from BP to MoS_2, and holes flow in the opposite direction, which causes the energy band of BP to bend upward and that of MoS_2 to bend in the opposite direction. As shown in Fig. 1(b–i), when $V_{ds} > 0$ (forward bias) is applied to the sensor, the carriers are free to cross the interface of heterojunction, which is more conducive to carrier transport. However, when $V_{ds} < 0$ (reverse bias) is applied, the carriers in MoS_2 and BP are blocked at the interface of heterojunction due to the existence of potential barriers, leading to a low current at reverse bias. Thus, three different operating modes may occur in diode-type gas sensors based on MoS_2/BP heterojunction (Text S1, Supporting Information). According to the diagram of the device structure, we prepared the MoS_2/BP heterojunctions employing the all-dry transfer method, as shown in Fig. S1a and Text S2. Fig. S1b shows an optical microscope image of the heterojunction, where the orange outline represents the MoS_2 region, and the green one represents the BP region. Atomic force microscopy (AFM) was used to analyze the high profile of the MoS_2/BP heterojunction and to measure the thickness and surface morphology. The flat and smooth surfaces can be identified by the AFM image (Fig. S1c). The thickness of the MoS_2 nanoflake is ≈ 99.1 nm, and that of the BP nanoflake is ≈ 95.7 nm (the inset of Fig. S1c).

The Raman spectra of individual MoS_2, BP, and MoS_2/BP heterojunction are shown in Fig. S1d. The MoS_2 nanoflake shows the characteristic peaks at 381.4 cm^{-1} ($E_{2\,g}$ mode) and 406.4 cm^{-1} ($A_{1\,g}$ mode) (bottom curve) and the BP nanoflake exhibits three peaks at 359.1 cm^{-1} ($A_{1\,g}$), 436.9 cm^{-1} ($B_{2\,g}$), and 464.5 cm^{-1} (A_g^2) (middle curve) [29,30]. The MoS_2/BP sample (top curve) shows all the characteristic peaks of the single MoS_2 and BP nanoflakes without any other peaks, which confirmed that neither MoS_2 nor BP was damaged and no other impurities were introduced into the sample during preparation. Besides, in the overlapping region of the MoS_2/BP heterojunction, the feature peaks of MoS_2 and BP are both observed in the Raman spectra, and there are nearly no shifts compared to that of the pure MoS_2 or BP films, indicating that the MoS_2 and BP films remain undamaged after the formation of the heterojunction. Figs. S1e, and f show the Raman mapping on the peak intensity of MoS_2 $A_{1\,g}$ and BP $B_{2\,g}$, respectively, which indicate the uniform structure of MoS_2/BP. As shown in Fig. S1g, in the region of MoS_2 and heterojunction, two prominent emission peaks can be found at 632 nm (1.96 eV) and 686 nm (1.81 eV), corresponding to the band gap transition from the lowest conduction bands to the highest valence band caused by spin-orbital splitting at K′ (K) points, respectively [31]. We can clearly observe the quenching effect of PL at the heterostructure area, indicating the efficient separation and transition of photo-generated electrons and holes, which result in the increase of non-radiative recombination and the decrease of PL emission recombination [32]. Thus, the Raman and PL spectra in Figs. S1d-g provide

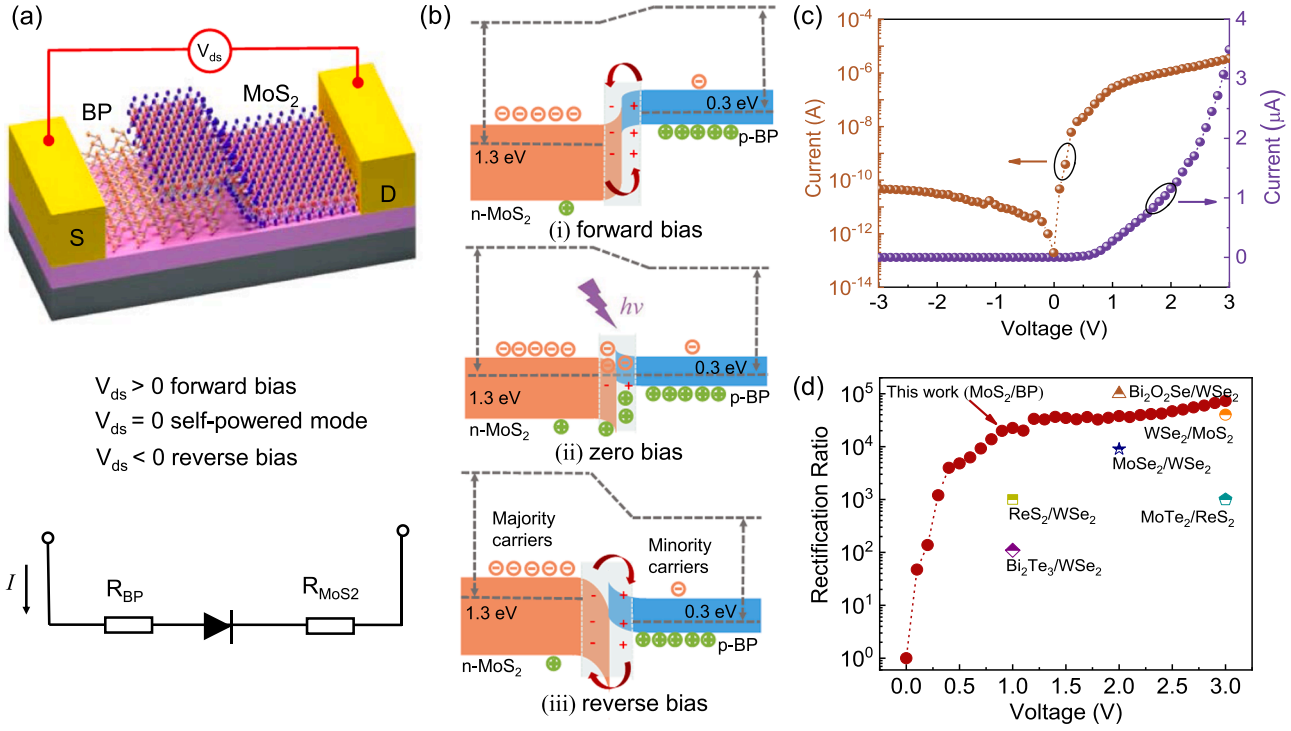

Fig. 1. a) Schematic diagram of the device structure and equivalent circuit diagram b) Schematic of the band diagrams of MoS_2/BP heterojunction under i) forward bias, ii) zero bias with illumination, and iii) reverse bias. c) I–V curves of the heterojunction in dark; d) Comparison of rectification ratio between this work with different 2d heterojunctions reported in the literature.

evidence for the formation of heterojunctions as well as strong coupling effects between the two materials.

3.2. Electrical and photoelectric properties

The p-n junction served as the basis for optoelectronic and microelectronic devices with interesting properties such as rectification behavior. First of all, we obtained the conductivity types of individual MoS_2 and BP as n- and p-types, respectively, by measuring the transfer characteristics (Fig. S2a, S3a, and Text S3 in Supporting Information). The dependence of I_{ds} on V_{gs} was weak due to Thomas-Fermi charge shielding in the thick BP nanoflake [22]. One of the most important parameters for evaluating the quality of a diode is the rectification ratio. Thus, we investigated the electrical characteristics of the MoS_2/BP heterojunction in the dark state, as shown in Fig. 1c. Our devices based on n-MoS_2/p-BP heterojunction exhibit strong rectification behavior, indicating good heterojunction interfaces. The rectification ratio ($|I_{forward}/I_{reverse}|$) increases rapidly and saturates with increasing $|V_{ds}|$, eventually reaching $7 * 10^4$ at $|V_{ds}| \approx 3$ V, which was competitive with reported heterojunctions based on 2D materials like Bi_2O_2Se/WSe_2 [33], WSe_2/MoS_2 [34], $MoTe_2/ReS_2$ [35], ReS_2/WSe_2 [36], $MoSe_2/WSe_2$ [37] and Bi_2Te_3/WSe_2 [38], as shown in Fig. 1d.

The optoelectronic properties of MoS_2/BP heterojunctions were further investigated as shown in Fig. 2. The photogenerated electrons and holes in the MoS_2 and BP layers under illumination were separated and transferred to different materials by an external electric field or a built-in electric field at the interface, and an additional current, called photocurrent I_{ph} (the difference between the current with and without illumination), was generated. In Fig. 2a, we present the log-scale I–V curves under dark, different power intensity of 405 nm laser, and 10 mW·cm^{-2} of a different wavelength from –3 to + 3 V. The I_{ph} grows with the increase in light power density due to the separation of the electron-hole pairs by the applied drain-source bias voltage. The ideality factor (n) was calculated to be 4.19 and 6.71 for the heterojunction in dark and under 405 illumination (Detailed calculation process in Fig. S4 and Text S4 of Supporting Information). As shown in Fig. 2b, the MoS_2/BP heterojunction demonstrates rapid and stable photoresponse from 405 to 635 nm. In addition, we introduced a key parameter, the optical responsivity (R) to evaluate the photosensitivity of the sensor, which was defined as in Eq. 1:

$$R = I_{ph}/P_{in} * S \quad (1)$$

The device area (S) was calculated from Fig. S1b to be approximately 200 μm^2. Thus, at an illumination power of 10 mW·cm^{-2} and a voltage bias of 3 V, the R of the heterojunction was about 94, 71, and 38 A·····W^{-1} for 405 nm, 532 nm, and 633 nm wavelengths, respectively (Fig. 2c). The photoresponse at 405 nm illumination was higher than that at 532 and 633 nm illumination, indicating that the heterojunction was more sensitive to 405 nm illumination. The responsivity of our device was one to two orders of magnitude larger than that of some 2D heterojunctions, such as the BP/WSe_2 and MoS_2/GaSe heterojunctions [25,39]. To illustrate more clearly the open-circuit voltage (V_{oc}) and short-circuit current (I_{sc}) at different incident light wavelengths and optical power densities, Fig. 2d shows the I-V curves zoomed in the results of Fig. 2a. The photogenerated carriers at the interface of MoS_2 and BP were separated into photogenerated electron-hole pairs under the built-in electric field, forming the short-circuit current (I_{sc}), which was characteristic of the photovoltaic effect. Both I_{sc} and V_{oc} increase as the incident optical power increases. The V_{oc} values of the junction were about 0.23, 0.33, and 0.36 V for optical power densities of 2, 6, and 10 mW·cm^{-2} at 405 nm illumination, respectively. The periodic switching I_{ph} of the device does not attenuate significantly (Fig. 2e), which ensures that the photovoltaic response of our MoS_2/BP heterostructure device has good stability and reproducibility. The electrical power (P_{el}) generated by the MoS_2/BP device at different wavelengths and power intensities was extracted from Eq. 2 (Fig. 2f):

$$P_{el} = I_{ds} \cdot V_{ds} \quad (2)$$

At 405 nm illumination, P_{el} increases with increasing optical power intensity to 90 pW. The formation of V_{oc} and I_{sc} provides the

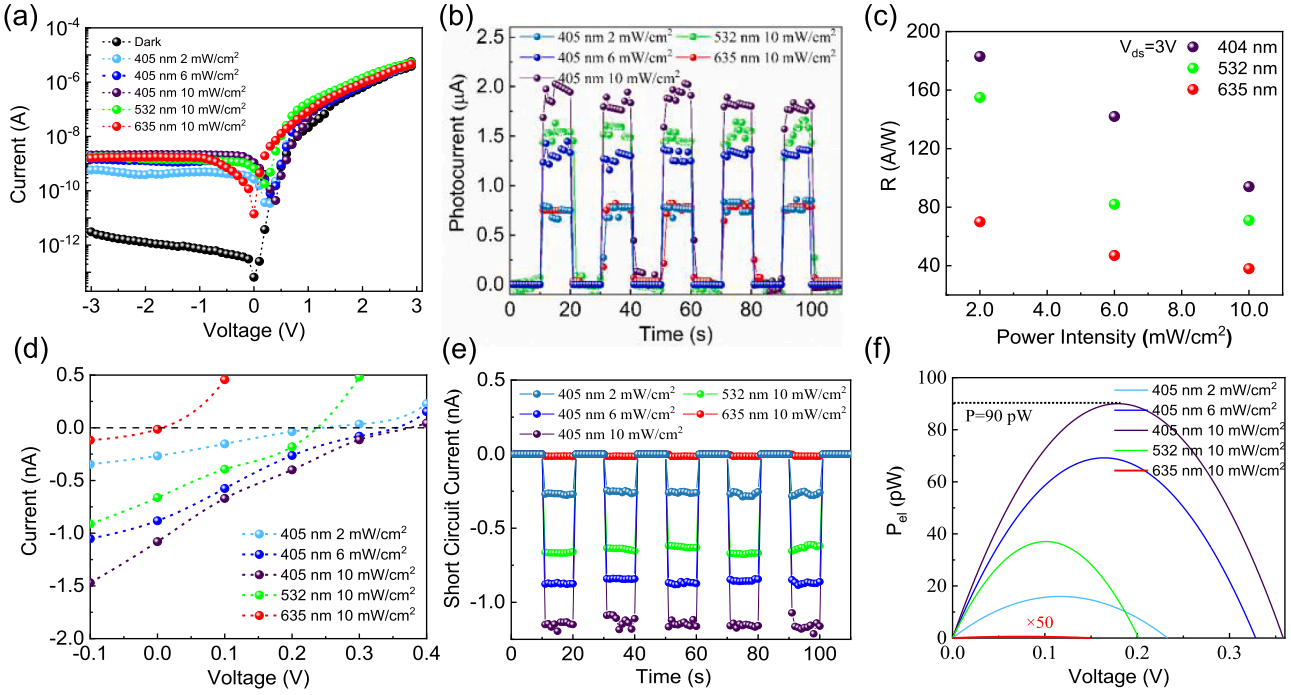

Fig. 2. Photoresponse characteristics of MoS_2/BP heterojunction. a) I_{ds}–V_{ds} measurements under visible light wavelengths (405, 532, and 635 nm) with different laser powers intensity for MoS_2/BP heterojunction. b) Dynamic photoresponse of the heterojunction under different visible light wavelengths. c) Responsivity of MoS_2/BP heterojunction under varied light intensities of different visible light wavelengths. d) Enlarged I_{ds}–V_{ds} measurements of Fig. 2a. e) Time-resolved photovoltaic response of the heterostructure at $V_{ds} = 0$ V. f) Electrical power generated by the MoS_2/BP heterojunction as a function of V_{ds}.

prerequisite for low-consumption self-powered gas sensors.

3.3. Gas sensing performance

Next, we placed individual MoS_2 and BP into the gas chamber to investigate their gas-sensing properties as shown in Figs. S2, S3, and Text S3. We investigated the above diode-type gas sensor based on n-type MoS_2/p-type BP heterojunction to verify the gas sensitivity of the heterojunction. All tests were performed at room temperature and atmospheric pressure. Fig. 3a shows the I-V curves of the heterojunction for different NO_2 concentrations without illumination. The current tends to decrease with increasing NO_2 concentration since the NO_2 molecule acts as an acceptor to capture electrons in the conduction band of the materials, resulting in the formation of the electron depletion layer [40]. As the number of adsorbed NO_2 molecules increases, the width of the electron-depletion layer will become wider, thus narrowing the electron-conducting channels of the MoS_2 in the heterojunction, and the sensor will gradually exhibit a decrease in current. Fig. S5 shows the current transients of the heterojunction to 100 ppm NO_2 at different bias voltages (Detailed description in Text S5), and Fig. S6 shows the current transients of MoS_2/BP heterojunction to 100 ppm of NO_2 under different light illumination with the wavelengths of 405 nm, 532 nm and 635 nm at self-powered mode (Text S6).

Fig. 3b shows the dynamic response transients of the heterojunction derived from Fig. S7 with the NO_2 concentrations of 100, 50, 20, 10, 5, 2, and 1 ppm at 3 V bias voltage (bottom curve), 0 V under 405 nm illumination of 10 mW·cm^{-2} (middle curve), and –3 V reverse bias (top curve). The gas sensing response declines monotonically as the concentration decreases from 100 ppm to 1 ppm, and the p-n junction gas sensor exhibits good response and recovery characteristics at 3 V bias voltage and 0 V under 405 nm illumination of 10 mW·cm^{-2}. However, at –3 V reverse bias, the current cannot be fully recovered after the NO_2 is removed, which can be ascribed to the block of carrier transport due to the spreading of the space charge region. As shown in Fig. S8, we summarized the dependence of the response on concentration from Fig. 3b. When the NO_2 concentration increased to 20 ppm, the response value raised rapidly, while at higher levels (above 20 ppm), the response tended to enhance slowly due to the saturation of NO_2 molecules on the sensor surface, and a dynamic equilibrium state between re-adsorbed and consumed gas can be achieved [41]. Moreover, these data points followed the Langmuir adsorption isotherm with respect to molecules adsorbed on the surface, with Eqs. 3–5:

$$R=426\cdot4/(1+37\cdot3/C) \text{ at } 3 \text{ V} \quad (3)$$

$$R=96\cdot1/(1+64\cdot9/C) \text{ at } -3 \text{ V} \quad (4)$$

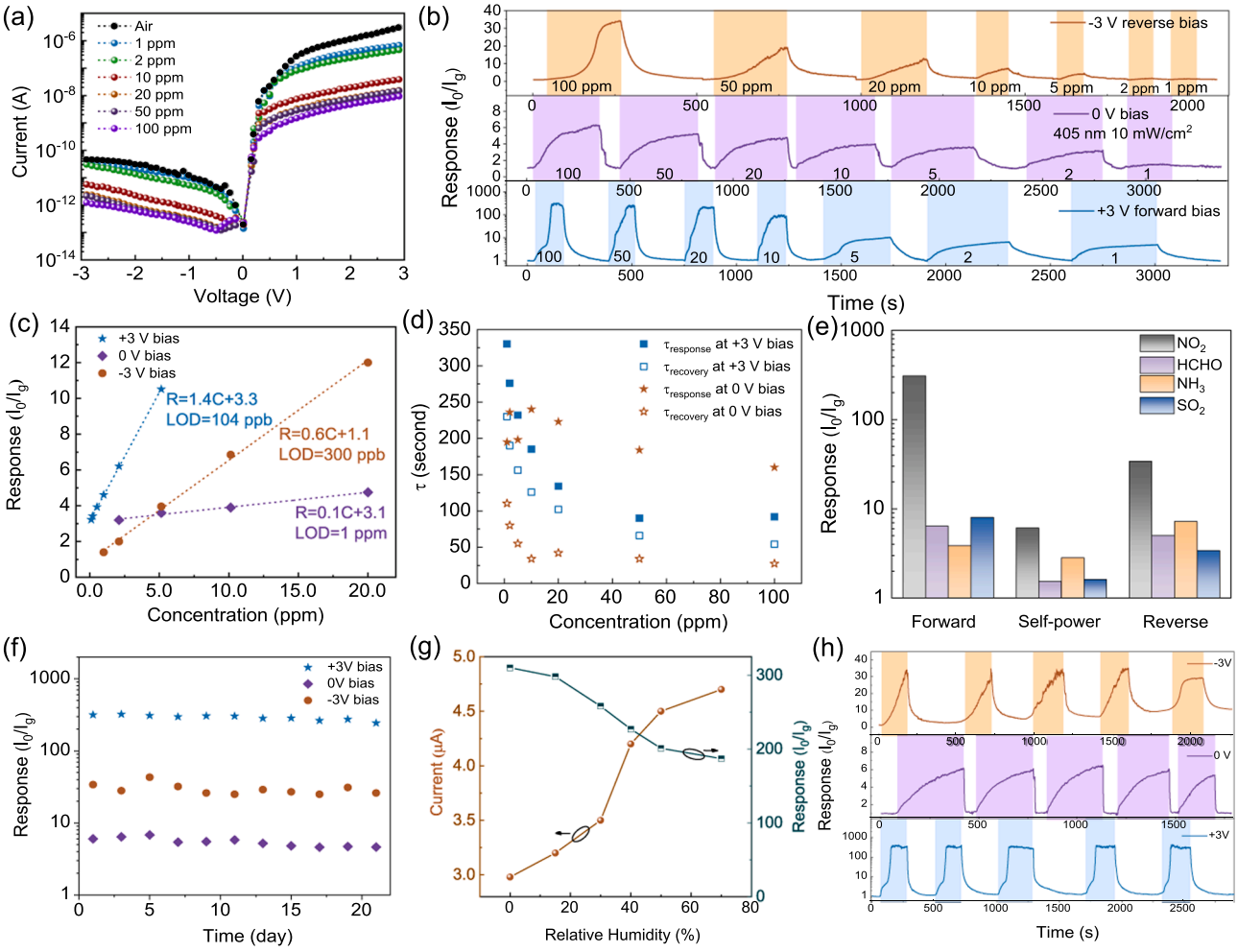

Fig. 3. Gas sensing characteristics of MoS_2/BP heterojunction. a) The I-V curve of MoS_2/BP heterojunction to different concentrations of NO_2 from 1 to 100 ppm at room temperature; b) The response transients of MoS_2/BP heterojunction to different concentrations of NO_2 from 100 to 1 ppm at 3 V (bottom curve), 0 V under 405 nm illumination of 10 mW·cm^{-2} (middle curve); and –3 V (top curve); c) Response of the MoS_2/BP in different concentration ranges of NO_2, and the dotted line represents the linear relationship between response and concentration; d) The response and recovery time at 3 V and 0 V bias extracted from Fig. 3d; e) Response of the sensors to 100 ppm of various gases; f) Long-term stability of the sensor to 100 ppm NO_2; g) The current and response curves of the MoS_2/BP sensor to 100 ppm NO_2 at various relative humidity; h) The reproducibility of the MoS_2/BP heterojunction gas sensor to 100 ppm NO_2.

$$R=5{\cdot}8/(1+2{\cdot}7/C) \text{ at } 0 \text{ V} \quad (5)$$

where C and R represent the target gas concentration and response, respectively. The fitting curve confirmed that the sensing mechanism was the absorption-induced charge transfer between the gas molecule and the heterojunction [23,42]. Fig. 3c displays the response of the sensor to 0.1–5 ppm NO_2 at 3 V, 1–20 ppm NO_2 at –3 V, and 2–20 ppm NO_2 at 0 V under 405 nm illumination of 10 $mW{\cdot}cm^{-2}$ at room temperature. These data points were analyzed by linear fitting to obtain the approximate equation (Eqs. 6–8):

$$R=1{\cdot}82\ C+3{\cdot}1 \text{ at } 3 \text{ V} \quad (6)$$

$$R=0{\cdot}1\ C+3{\cdot}1 \text{ at } 0 \text{ V} \quad (7)$$

$$R=0{\cdot}6\ C+1{\cdot}1 \text{ at } -3 \text{ V} \quad (8)$$

where S and C are the response of the sensor and the NO_2 concentration, respectively. The theoretical detection limit of the sensor was calculated to be 104 ppb at 3 V, 300 ppb at –3 V, and 1 ppm at 0 V for NO_2 (see Text S7 for a detailed calculation procedure). Compared with the previously reported 2D material gas sensors, our gas sensor is at an advanced level of gas sensitivity to ppb-level NO_2 at room temperature [43,44]. We have estimated the response time ($\tau_{response}$) and recovery time ($\tau_{recovery}$) for different concentrations of NO_2, as shown in Fig. 3d. The τ values decrease with increasing concentration of NO_2, indicating rapid adsorption and desorption of the gas at high concentrations. The $\tau_{recovery}$ was calculated to be 54 s at 3 V bias and 27.3 s at 0 V bias under 405 nm illumination, respectively. The ultra-fast recovery rate was attributed to the fast mobility of the photogenerated hole under the action of the built-in electric field (Eq. 9).

$$NO_2^-(ads)+h^+(hv)\rightarrow NO_2(gas) \quad (9)$$

It can be found from Fig. 3e, at +3 V forward bias, the sensor does not respond significantly to other gases such as ammonia, formaldehyde, and SO_2, indicating high selectivity of MoS_2/BP heterojunction for NO_2. The stability of gas sensor is a key factor in practical gas detection. As shown in Fig. 3f, the long-term stability of the sensor based on MoS_2/BP junction to 100 ppm NO_2 at 3 V, 0 V, and –3 V was measured at room temperature. The response only revealed about 27 % at 3 V, 30 % at 0 V, and 23 % at –3 V decay relative to the initial value after 3 weeks, indicating the reliable long-term stability of the sensors. Besides, ambient humidity has a great influence on gas-sensing performance. Fig. 3g shows the variation of current and response to 100 ppm nitrogen dioxide for the MoS_2/BP sensor at different relative humidity (0–70 %) at 25 °C. The response tended to decrease with increasing humidity. The sensor maintains a relatively good response even at relative humidity above 50 %. As shown in Fig. 3h, we studied the repeatability of the sensor at different voltage biases. When the sensor is repeatedly exposed to 100 ppm NO_2, the response-recovery transients do not change significantly at 3 V and 0 V, indicating that the reproducibility of the sensor is quite satisfactory.

In order to simulate the switching of operating modes in a real application environment, we present dynamic current transients of a MoS_2/BP heterojunction gas sensor for 100 ppm NO_2 under alternating signal stimulation in forward bias and 405 nm illumination of 10 $mW{\cdot}cm^{-2}$ in self-powered mode as shown in Fig. S9a-c (Detail description in Text S8–9). By combining the gas-sensing performance under alternating forward bias and self-powered operating modes, the diode-type gas sensor achieves the balanced properties of 100 ppm NO_2. Therefore, switching the two operating modes can expand the potential application field of the device.

To compare our device performance, we summarize the research on the NO_2 gas sensors in recent years as shown in Figs. S9d-e and Text S10. Our diode-based gas sensor at self-powered mode has a high response of approximately 6.25 (1.44) to 100 (1) ppm NO_2 at room temperature, and the fast recovery speed compared to other self-powered gas sensors. More importantly, our gas sensors are able to quickly switch between forward bias and self-powered modes, which is a feature not available in most gas sensors. Thus, the fast recovery and repeatable operation, combined with the sensitivity to low concentrations (100 ppb) of NO_2, demonstrate the potential of our gas sensors to develop highly sensitive, sustainable, low power consumption, and reliable gas sensing platforms.

3.4. Gas sensing mechanism

To probe the NO_2 sensing mechanism of the MoS_2/BP heterojunction, we employed Raman and PL spectra before and after NO_2 exposure at room temperature. The in-plane ($E_{2\,g}$) and out-of-plane ($A_{1\,g}$) vibrational modes of MoS_2 with peak positions at 383.7 and 408.7 cm^{-1} before NO_2 exposure are shown in Fig. 4a. However, upon exposure to NO_2, the $E_{2\,g}$ peaks were red-shifted by 2.7 cm^{-1} and the intensity was enhanced compared to MoS_2 without NO_2, suggesting a decrease in the electron concentration of the nanoflakes [31]. To further evaluate the effect of NO_2 adsorption on MoS_2/BP heterojunction, we have extracted the PL spectra from MoS_2/BP before and after NO_2 exposure as well. As shown in Fig. 4b, before exposure to NO_2, two prominent emission peaks can be identified at 632 nm (1.96 eV) and 685.4 nm (1.81 eV) respectively. However, a significant blue shift and quenching at 681.6 nm (1.82 eV) were observed after exposure to NO_2, which was generally ascribed to the p-doping from NO_2 [45]. Thus, these phenomena suggest that NO_2 adsorbed on the MoS_2/BP junction surface acts as an electron acceptor.

Kelvin probe force microscopy (KPFM) was used to experimentally study the charge transfer and Fermi energy level shift processes before and after NO_2 exposure. The contact potential difference (CPD), i.e., the surface potential difference, is determined by the difference in the work function between the AFM tip (W_{tip}) and the sample (W_{sample}), with Eq. 10:

$$CPD=(W_{tip}-W_{sample})/e \quad (10)$$

Where e is the fundamental charge. We calculated the surface potential of the heterojunction before and after exposure to NO_2. As shown in Fig. 4c and d, the surface potential difference of the heterojunction increases to 305 mV from 180 mV after NO_2 exposure. Further, the work function of MoS_2 and BP can be calculated as 4.93 and 4.75 eV before NO_2 exposure, and 5.25 and 4.90 eV after NO_2 exposure respectively, demonstrating the shift of the Fermi energy level to the valence band. (Details of the calculation were shown in Fig. S10 and Text S11). The results indicated that electrons were transferred from the heterojunction to the NO_2 molecule.

The gas sensing mechanism can be explained by the energy band diagram of the MoS_2/BP heterojunction shown in Fig. S11 and Fig. 4e–f, including the bias voltage mode and the photovoltaic self-powered mode. The band gaps of multilayer MoS_2 and BP were 1.3 and 0.4 eV, respectively [46,47]. When the contact between n-type MoS_2 and p-type BP occurs, a type II p-n junction is expected to form at the interface, which regulates the carrier transport between the two materials. Electrons are expected to transfer from p-type BP to n-type MoS_2, leaving a positively charged region at the BP interface and forming a depletion layer; similarly, holes at the p-n junction interface move from n-type MoS_2 to p-type BP, forming a negatively charged region at the other side. Finally, the energy band bends are formed until the Fermi energy level of the p-n junction reaches equilibrium, as shown in Fig. S11b. Under forward bias, the carriers are free to cross the interface of heterojunction, which causes the electron to be more easily trapped by NO_2 (Fig. 4e), and therefore the gas sensor at forward bias may exhibit high sensitivity. Under light illumination, the separation of photogenerated electron-hole pairs produces a short-circuit current. Due to the strong electron affinity of NO_2, electron can be easily trapped from the conduction band of the materials (Fig. 4f). Thus, the results show that the short-circuit current I_{sc} of the heterojunction decreases significantly

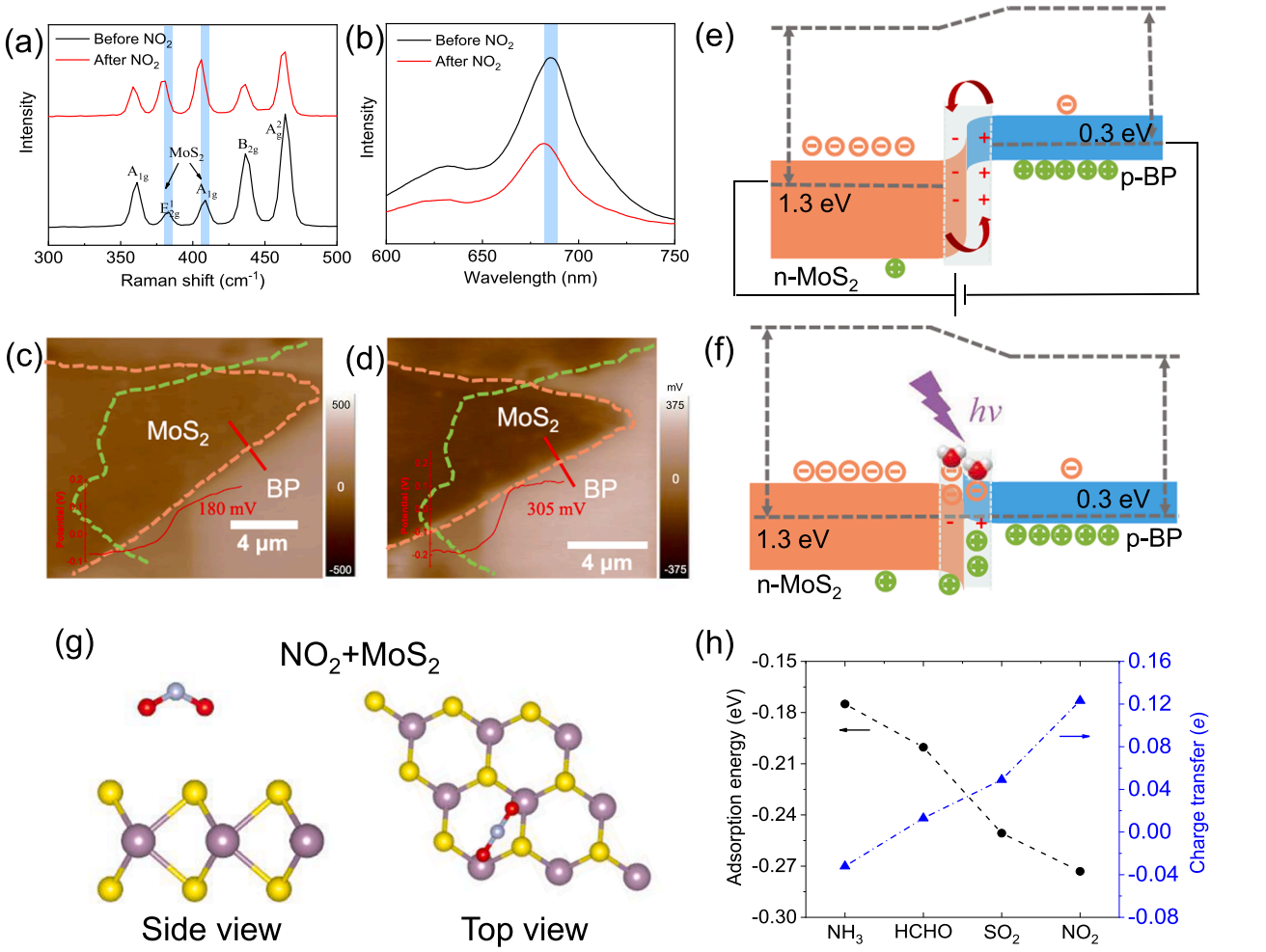

Fig. 4. The gas sensing mechanism of MoS_2/BP heterojunction for NO_2. a) Raman spectra and b) PL spectra of the heterojunction before and after NO_2 exposure at room temperature; KPFM images of the heterojunction c) before and d) after exposing to NO_2; Band diagram of e) the heterojunction at forward bias voltage, f) and heterojunction with NO_2 exposure under light illumination. g) The adsorption structure with geometric binding configuration for the model of NO_2 on the MoS_2 nanosheets. h) The adsorption energies (E_a), and Bader charge transfer ($\Delta q(e)$) of the gas molecules adsorbed on MoS_2.

after NO_2 exposure.

We also constructed the atomic structure of MoS_2 and its gas adsorption configuration, and carried out DFT simulation on the gas sensor based on MoS_2 to deeply understand the gas sensing mechanism. The BP under MoS_2 has a negligible effect on the adsorption behaviors of gas molecules on MoS_2. Therefore, we model the adsorption structure by only considering the effect of MoS_2. The typical adsorption sites on MoS_2 are considered, including the Mo site, S site, and hollow site, as shown in Fig. S12. Through complete geometric optimization, the most stable adsorption system in each case is obtained, as shown in Fig. 4g and S13. The adsorption energy E_a is introduced in order to qualitatively analyze the interaction between MoS_2 and gas molecules, which is expressed by the following Eq. 11:

$$E_a = E_{MoS2+gas} - E_{gas} - E_{MoS2} \quad (11)$$

where $E_{MoS2+gas}$, E_{gas}, and E_{MoS2} are the total energy of the single gas molecule adsorption on MoS_2, gas molecules, and MoS_2, respectively. The adsorption energies (E_a) for the gases on the different adsorption sites are shown in Table S1 (Supporting Information). And we sorted out the adsorption energies and Bader charge transfer ($\Delta q(e)$) of the most stable adsorption configuration, as shown in Fig. 4h. We find that the adsorption energy of NO_2 on MoS_2 is larger than other adsorption systems. When a NO_2 molecule is adsorbed onto MoS_2, the charge transfer from MoS_2 to NO_2 is 0.123e, resulting in p-type doping on the MoS_2, which again demonstrates the strongest absorption strength of NO_2 on MoS_2. Therefore, our calculation results are consistent with our experiments in that the devices show good selectivity to NO_2.

4. Conclusions

In summary, we proposed a diode-type gas sensor based on MoS_2/BP heterojunction exhibiting multiple operating modes at room temperature. In forward bias voltage, the gas sensor possesses a relatively high response (R=310), reversibility, and selectivity. In the self-powered mode, the separation of photogenerated carriers under the action of the built-in electric field provides the electric power for the device under light illumination. Thus, the gas sensor shows favorable reversibility, LOD of 1 ppm, and a faster recovery rate (27.3 s). Accordingly, through the alternating operation of forward bias and self-powered modes of operation, the diode-type gas sensor achieves the balanced properties of high response, repeatable operation, and fast recovery to 100 ppm NO_2 at room temperature. The electron transfer between the heterojunction and NO_2 molecules at different operation modes was confirmed as the main mechanism of NO_2 sensitivity by KPFM, Raman, and PL spectra before and after NO_2 exposure. The DFT simulations explain the gas-sensing mechanism of MoS_2 at the atomic scale. Charge transfer analysis shows that the decrease in conductivity of MoS_2 after the adsorption of NO_2 can be attributed to interfacial electron transfer from MoS_2 to

NO_2. The 2D heterojunctions present promising gas sensing performance in the dual operating modes and hold the potential as a novel sensing platform for low-power environmental monitoring systems.

CRediT authorship contribution statement

Nan Zhang: Conceptualization, Methodology, Writing – original draft, Validation, Funding acquisition. **Fan Tan**: Conceptualization, Methodology, Visualization. **Liujian Qi**: Software, Resources, Investigation, Funding acquisition. **Junru An**: Investigation, Visualization. **Mengqi Che**: Conceptualization, Methodology. **Yaru Shi** and **Yahui Li**: Investigation, Visualization. **Xiaojuan Sun**: Investigation, Visualization. **Zhiming Shi**: Software; **Shaojuan Li**: Supervision, Conceptualization, Writing – review & editing, Project administration, Supervision, Funding acquisition. **Dabing Li**: Funding acquisition, Project administration.

Declaration of Competing Interest

The authors declare that they have no known competing financial interests or personal relationships that could have appeared to influence the work reported in this paper.

Data Availability

Data will be made available on request.

Acknowledgements

We acknowledge the financial support from the National Natural Science Foundation of China (No. 62022081 and 61974099), the Science Fund for Creative Research Groups of the National Natural Science Foundation of China (No. 62121005), the National Key Research and Development Program (2021YFA0717600), the Natural Science Foundation of Jilin Province (20210101173JC and 20220508030RC), China Postdoctoral Science Foundation (2021TQ0358 and 2021M703128) and Changchun Key Research and Development Program (21ZY03).

Appendix A. Supporting information

Supplementary data associated with this article can be found in the online version at doi:10.1016/j.snb.2023.134620.

References

[1] H. Tabata, H. Matsuyama, T. Goto, O. Kubo, M. Katayama, Visible-light-activated response originating from carrier-mobility modulation of NO_2 Gas sensors based on MoS_2 monolayers, ACS Nano 15 (2021) 2542–2553.
[2] T. Liang, Z. Dai, Y. Liu, X. Zhang, H. Zeng, Suppression of Sn^{2+} and Lewis acidity in SnS2/black phosphorus heterostructure for ppb-level room temperature NO_2 gas sensor, Sci. Bull. 66 (2021) 2471–2478.
[3] P.H. Tan, C.H. Hsu, Y.C. Shen, C.P. Wang, K.L. Liou, J.R. Shih, et al., Complementary metal-oxide-semiconductor compatible 2D layered film-based gas sensors by floating-gate coupling effect, Adv. Funct. Mater. 32 (2022), 2108878.
[4] R.A. Potyrailo, Multivariable sensors for ubiquitous monitoring of gases in the era of internet of things and industrial internet, Chem. Rev. 116 (2016) 11877–11923.
[5] Z.L. Song, W.H. Ye, Z. Chen, Z.S. Chen, M.T. Li, W.Y. Tang, et al., Wireless self-powered high-performance integrated nanostructured-gas-sensor network for future smart homes, ACS Nano 15 (2021) 7659–7667.
[6] L. Yang, G. Zheng, Y. Cao, C. Meng, Y. Li, H. Ji, et al., Moisture-resistant, stretchable NO_x gas sensors based on laser-induced graphene for environmental monitoring and breath analysis, Microsyst. Nanoeng. 8 (1) (2022) 12.
[7] D.Y. Wang, D.Z. Zhang, Y. Yang, Q. Mi, J.H. Zhang, L.D. Yu, Multifunctional latex/polytetrafluoroethylene-based triboelectric nanogenerator for self-powered organ-like MXene/metal-organic framework-derived CuO nanohybrid ammonia sensor, ACS Nano 15 (2021) 2911–2919.
[8] C. Li, P.G. Choi, Y. Masuda, Highly sensitive and selective gas sensors based on NiO/MnO_2@ NiO nanosheets to detect allyl mercaptan gas released by humans under psychological stress, Adv. Sci. 9 (2022), 2202442.
[9] P. Devi, S. Sharma, R. Saini, Room-temperature gas-sensing properties of metal oxide nanowire/graphene hybrid structures, 1D semiconducting hybrid nanostructures: synthesis and applications in gas sensing and optoelectronics (2023) 57–74.
[10] W.Y. Tang, Z.S. Chen, Z.L. Song, C. Wang, Z.A. Wan, C.L.J. Chan, et al., Microheater integrated nanotube array gas sensor for parts-per-trillion level gas detection and single sensor-based gas discrimination, ACS Nano 16 (2022) 10968–10978.
[11] W. Xin, X.K. Li, X.L. He, B.W. Su, X.Q. Jiang, K.X. Huang, et al., Black-phosphorus-based orientation-induced diodes, Adv. Mater. 30 (2018), 1704653.
[12] S. Jia, Z.H. Jin, J. Zhang, J.T. Yuan, W.B. Chen, W. Feng, et al., Lateral monolayer $MoSe_2$-WSe_2 p-n heterojunctions with giant built-in potentials, Small 16 (2020), 2002263.
[13] C. Jia, S.X. Wu, J.Z. Fan, C.J. Luo, M.H. Fan, M. Li, L.P. He, Y.J. Yang, H. Zhang, Ferroelectrically modulated and enhanced photoresponse in a self-powered α-In_2Se_3/Si heterojunction photodetector, ACS Nano 17 (2023) 6534–6544.
[14] S.M. Majhi, A. Mirzaei, H.W. Kim, S.S. Kim, T.W. Kim, Recent advances in energy-saving chemiresistive gas sensors: a review, Nano Energy 79 (2021), 105369.
[15] L. Li, G. Gao, X.T. Liu, Y.M. Sun, J.P. Lei, Z.C. Chen, et al., Polarization-resolved p-Se/n-WS_2 heterojunctions toward application in microcomputer system as multivalued signal trigger, Small 18 (2022), 2202523.
[16] S. Niu, Y. Hu, X. Wen, Y. Zhou, F. Zhang, L. Lin, et al., Enhanced performance of flexible ZnO nanowire based room-temperature oxygen sensors by Piezotronic effect, Adv. Mater. 25 (2013) 3701–3706.
[17] T. Knobloch, On the Electrical Stability of 2D Material-Based Field-Effect Transistors, TU Wien Vienna, Austria, 2022.
[18] A.M. Afzal, M.Z. Iqbal, G. Dastgeer, G. Nazir, S. Mumtaz, M. Usman, J. Eom, WS_2/GeSe/WS_2 bipolar transistor-based chemical sensor with fast response and recovery times, ACS Appl. Mater. Interfaces 12 (2020) 39524–39532.
[19] T. Kim, T.H. Lee, S.Y. Park, T.H. Eom, I. Cho, Y. Kim, et al., Drastic gas sensing selectivity in 2-dimensional MoS_2 nanoflakes by noble metal decoration, ACS Nano 17 (2023) 4404–4413.
[20] E. Lee, A.V. Mohammadi, B.C. Prorok, Y.S. Yoon, M. Beidaghi, D.J. Kim, Room temperature gas sensing of two-dimensional titanium carbide (MXene), ACS Appl. Mater. Interfaces 9 (2017) 37184–37190.
[21] F. Wang, Z.X. Wang, K. Xu, F.M. Wang, Q.S. Wang, Y. Huang, et al., Tunable GaTe-MoS_2 van der Waals p-n Junctions with novel optoelectronic performance, Nano Lett. 15 (2015) 7558–7566.
[22] Z. Feng, B. Chen, S. Qian, L. Xu, L. Feng, Y. Yu, et al., Chemical sensing by band modulation of a black phosphorus/molybdenum diselenide van der Waals heterostructure, 2D Mater. 3 (2016), 035021.
[23] W. Zheng, Y. Xu, L. Zheng, C. Yang, N. Pinna, X. Liu, et al., MoS_2 Van der Waals p–n junctions enabling highly selective room-temperature NO_2 sensor, Adv. Funct. Mater. 30 (2020), 2000435.
[24] Y. Kim, S. Lee, J.G. Song, K.Y. Ko, W.J. Woo, S.W. Lee, M. Park, H. Lee, Z. Lee, H. Choi, 2D transition metal dichalcogenide heterostructures for p-and n-type photovoltaic self-powered gas sensor, Adv. Funct. Mater. 30 (2020), 2003360.
[25] Y. Niu, J.W. Zeng, X.C. Liu, J.L. Li, Q. Wang, H. Li, et al., A photovoltaic self-powered gas sensor based on all-dry transferred MoS_2/GaSe heterojunction for ppb-level NO_2 sensing at room temperature, Adv. Sci. 8 (2021), 2100472.
[26] G. Kresse, D. Joubert, From ultrasoft pseudopotentials to the projector augmented-wave method, Phys. Rev. B 59 (1999) 1758.
[27] P.E. Blöchl, Projector augmented-wave method, Phys. Rev. B 5 (1994) 17953.
[28] S. Grimme, J. Antony, S. Ehrlich, H. Krieg, A consistent and accurate ab initio parametrization of density functional dispersion correction (DFT-D) for the 94 elements H-Pu, J. Chem. Phys. 132 (2010), 154104.
[29] L. Sun, H. Hu, D. Zhan, J. Yan, L. Liu, J.S. Teguh, et al., Plasma modified MoS_2 nanoflakes for surface enhanced Raman scattering, Small 10 (2014) 1090–1095.
[30] H.B. Ribeiro, M.A. Pimenta, C.J. de Matos, Raman spectroscopy in black phosphorus, J. Raman Spectrosc. 49 (2018) 76–90.
[31] B. Birmingham, J. Yuan, M. Filez, D. Fu, J. Hu, J. Lou, et al., Probing the effect of chemical dopant phase on photoluminescence of monolayer MoS_2 using in situ Raman microspectroscopy, J. Phys. Chem. C. 123 (2019) 15738–15743.
[32] B.M. Bersch, Electronic Transport in Synthetic Transition Metal Dichalcogenides and Novel Graphene/Metal Heterostructures, The Pennsylvania State University,, 2019.
[33] P. Luo, F. Wang, J. Qu, K. Liu, X. Hu, K. Liu, T. Zhai, Self-driven WSe2/Bi2O2Se van der Waals heterostructure photodetectors with high light on/off ratio and fast response, Adv. Funct. Mater. 31 (2021), 2008351.
[34] H.S. Lee, J. Ahn, W. Shim, S. Im, D.K. Hwang, 2D WSe_2/MoS_2 van der Waals heterojunction photodiode for visible-near infrared broadband detection, Appl. Phys. Lett. 113 (2018), 163102.
[35] J. Ahn, J.-H. Kyhm, H.K. Kang, N. Kwon, H.-K. Kim, S. Park, et al., 2D $MoTe_2$/ReS_2 van der Waals heterostructure for high-performance and linear polarization-sensitive photodetector, ACS Photonics 8 (2021) 2650–2658.
[36] A. Varghese, D. Saha, K. Thakar, V. Jindal, S. Ghosh, N.V. Medhekar, et al., Near-direct bandgap WSe_2/ReS_2 type-II pn heterojunction for enhanced ultrafast photodetection and high-performance photovoltaics, Nano Lett. 20 (2020) 1707–1717.
[37] H. Xue, Y. Wang, Y. Dai, W. Kim, H. Jussila, M. Qi, et al., A $MoSe_2$/WSe_2 heterojunction-based photodetector at telecommunication wavelengths, Adv. Funct. Mater. 28 (2018), 1804388.
[38] H. Liu, X. Zhu, X. Sun, C. Zhu, W. Huang, X. Zhang, et al., Self-powered broad-band photodetectors based on vertically stacked WSe_2/Bi_2Te_3 p-n heterojunctions, ACS Nano 13 (2019) 13573–13580.
[39] J. Sun, Y. Wang, S. Guo, B. Wan, L. Dong, Y. Gu, C. Song, C. Pan, Q. Zhang, L. Gu, Lateral 2D WSe_2 p–n homojunction formed by efficient charge-carrier-type modulation for high-performance optoelectronics, Adv. Mater. 32 (2020), 1906499.

[40] J.Z. Ou, W.Y. Ge, B. Carey, T. Daeneke, A. Rotbart, W. Shan, Yet, et al., Physisorption-based charge transfer in two-dimensional SnS_2 for selective and reversible NO_2 gas sensing, ACS Nano 9 (2015) 10313–10323.
[41] L. Zhou, C. Yang, W. Zhu, R. Li, X. Pang, Y. Zhen, et al., Boosting alkaline hydrogen evolution reaction via an unexpected dynamic evolution of molybdenum and selenium on $MoSe_2$ electrode, Adv. Energy Mater. 12 (2022), 2202367.
[42] R. Kumar, R.N. Jenjeti, S. Sampath, Two-dimensional, few-layer $MnPS_3$ for selective NO_2 gas sensing under ambient conditions, ACS Sens 5 (2020) 404–411.
[43] S. Dhara, H. Jawa, S. Ghosh, A. Varghese, D. Karmakar, S. Lodha, All-electrical high-sensitivity, low-power dual-mode gas sensing and recovery with a WSe_2/MoS_2 pn heterodiode, ACS Appl. Mater. Interfaces 13 (2021) 30785–30796.
[44] A. Di Bartolomeo, Emerging 2D materials and their Van Der Waals heterostructures, Nanomaterials 10 (2020) 579.
[45] K. Zhang, B.M. Bersch, J. Joshi, R. Addou, C.R. Cormier, C. Zhang, et al., Tuning the electronic and photonic properties of monolayer MoS_2 via in situ rhenium substitutional doping, Adv. Funct. Mater. 28 (2018), 1706950.
[46] L. Ye, H. Li, Z. Chen, J. Xu, Near-infrared photodetector based on MoS_2/black phosphorus heterojunction, ACS Photonics 3 (2016) 692–699.
[47] S.Y. Cho, Y. Lee, H.J. Koh, H. Jung, J.S. Kim, H.W. Yoo, J. Kim, H.T. Jung, Superior chemical sensing performance of black phosphorus: comparison with MoS_2 and graphene, Adv. Mater. 28 (2016) 7020–7028.

Nan Zhang received his Ph.D. degrees in Electronics Science and Technology from Jilin University, China, in 2021. Since 2016, his research interests have been focused on the nanomaterials in the field of gas sensing.

Fan Tan received his B.S. degrees from Chongqing University of Posts and Telecommunications in 2015. Now, he is currently studying for his Ph.D. degrees in Jilin University. His present works mainly focus on synthesis of solid state functional materials, gas sensors, and photoelectric devices.

Liujian Qi received his Ph.D degrees from Jilin University, China, in 2020. Since 2014, his main research interest is the theoretical calculation of nanomaterials.

Junru An received his Ph.D degrees from University of Chinese Academy of Sciences, China, in 2023. Since 2020, his main research interest is optoelectronic materials and devices.

Mingqi Che is an postgraduate in University of Chinese Academy of Sciences, China, and interested in nanomaterials and chemical sensors.

Yaru Shi is currently studying for his Ph.D degrees in University of Chinese Academy of Sciences, China. Since 2021, her research interests have been focused on the metal oxides nanomaterials and chemical sensors.

Yahui Li is currently studying for his Ph.D degrees in University of Chinese Academy of Sciences, China. Since 2017, her research interests have been focused on the optoelectronic materials and devices.

Zhiming Shi received the PhD degree from Jilin University and mainly devotes to the research of the first principles calculations.

Xiaojuan Sun is a professor in CIOMP. Her current research interests focus on synthesis of nanomaterials and application for gas sensor.

Shaojuan Li received the Ph.D degree from School of Information Science and Technology of Peking University in 2008. Now, she is a full professor in the CIOMP, and mainly devoted to the research of electronic functional materials and devices.

Dabing Li received the PhD degree from University of Chinese Academy of Sciences, now he is a professor majoring in optoelectronic materials and devices.